

Incommensurate antiferromagnetic fluctuations in single-crystalline LiFeAs studied by inelastic neutron scattering

N. Qureshi,^{1,*} P. Steffens,² D. Lamago,^{3,4} Y. Sidis,³ O. Sobolev,⁵ R. A. Ewings,⁶ L. Harnagea,⁷ S. Wurmehl,^{7,8} B. Büchner,^{7,8} and M. Braden^{1,†}

¹*II. Physikalisches Institut, Universität zu Köln, Zùlpicher Strasse 77, D-50937 Köln, Germany*

²*Institut Laue Langevin, BP156, 38042 Grenoble Cedex, France*

³*Laboratoire Léon Brillouin, CEA/CNRS, F-91191 Gif-sur-Yvette Cedex, France*

⁴*Institut für Festkörperphysik, Karlsruher Institut für Technologie (KIT), Postfach 3640, D-76121 Karlsruhe, Germany*

⁵*Institut für Physikalische Chemie, Georg-August-Universität Göttingen, Tammannstrasse 6, 37077 Göttingen, Germany*

⁶*ISIS Facility, Rutherford Appleton Laboratory, STFC, Chilton, Didcot, Oxon, OX11 0QX, United Kingdom*

⁷*Leibniz-Institute for Solid State Research, IFW-Dresden, 01171 Dresden, Germany*

⁸*Institut für Festkörperphysik, Technische Universität Dresden, D-01171 Dresden, Germany*

(Dated: July 2, 2014)

We present an inelastic neutron scattering study on single-crystalline LiFeAs devoted to the characterization of the incommensurate antiferromagnetic fluctuations at $\mathbf{Q} = (0.5 \pm \delta, 0.5 \mp \delta, q_l)$. Time-of-flight measurements show the presence of these magnetic fluctuations up to an energy transfer of 60 meV, while polarized neutrons in combination with longitudinal polarization analysis on a triple-axis spectrometer prove the pure magnetic origin of this signal. The normalization of the magnetic scattering to an absolute scale yields that magnetic fluctuations in LiFeAs are by a factor eight weaker than the resonance signal in nearly optimally Co-doped BaFe₂As₂, although a factor two is recovered due to the split peaks owing to the incommensurability. The longitudinal polarization analysis indicates weak spin space anisotropy with slightly stronger out-of-plane component between 6 and 12 meV. Furthermore, our data suggest a fine structure of the magnetic signal most likely arising from superposing nesting vectors.

PACS numbers:

Keywords:

I. INTRODUCTION

The interest in the FeAs-based superconductors¹ is ongoing after six years of extensive research as still no consensus has been achieved concerning the superconducting character and pairing mechanism. LiFeAs is special amongst the many FeAs-based superconductors, as superconductivity appears in the parent compound at elevated temperatures without doping or application of pressure. This particularity of LiFeAs most likely arises from its electronic structure with strongly reduced nesting between electron and hole Fermi-surface sheets as it was first deduced from angle-resolved photoemission spectroscopy (ARPES)². In the 1111 and 122 families (named after their stoichiometry) the Fermi nesting conditions are excellent stabilizing a spin density wave (SDW), which has to be suppressed by doping^{1,3–5} or the application of pressure⁶ in order to reach the superconducting state. LiFeAs does not exhibit any structural transition nor a magnetically ordered phase.^{7–9} Theoretical calculations¹⁰ explain this fact by its poor Fermi nesting properties and unusually shallow hole pockets around the Γ point, which is in agreement with ARPES experiments.^{11,12} The flat top of the hole pockets implies a large density of states around the Γ point and in combination with small-momentum scattering vectors within the inner hole pocket this would favor ferromagnetic fluctuations and a triplet pairing mechanism.¹⁰ The

symmetry of the order parameter has been a controversial subject, several reports using ARPES, quasiparticle interference (QPI) or theoretical approaches favor an s^\pm wave,^{13–15} while there is also support for a p -wave state.^{16–18} Although the calculations in Ref. 15 support an s^\pm wave state driven by collinear antiferromagnetic fluctuations, the authors state that ferromagnetic fluctuations stemming from the small hole pocket at the Γ point may dominate at higher energies and/or at higher temperatures. In our previous work¹⁹ we have established the energy and temperature dependence of an antiferromagnetic excitation located at an incommensurate position $\mathbf{Q} = (0.5 \pm \delta, 0.5 \mp \delta, q_l)$ resembling magnetic correlations in electron doped BaFe₂As₂. Similar results were obtained by Wang et al.²⁰ The origin of the magnetic signal has been interpreted as scattering between the electron pockets centered around the (π, π) point and either the outer²¹ or the inner²⁰ hole pockets around the zone center.

In this work we present a comprehensive inelastic neutron scattering (INS) study using different cold and thermal triple-axis spectrometers and a time-of-flight instrument devoted to extend the characterization of the incommensurate antiferromagnetic fluctuations in single-crystalline LiFeAs. We present the inelastic scattered neutron intensity in absolute units using two different techniques leading to perfectly agreeing results. The magnetic fluctuations have been investigated up to energy transfers of

80 meV and spin-space anisotropies have been studied by polarized neutrons with longitudinal polarization analysis (LPA). Furthermore, we have investigated $S(\mathbf{Q}, \omega)$ in a broad \mathbf{Q} - ω range to search for any ferromagnetic fluctuation at elevated temperatures and energy transfers.

II. EXPERIMENTAL

The same single crystal sample as in Ref. 19 has been used for all the experiments presented here. The normalization to an absolute intensity scale has been done with data obtained at the thermal triple-axis spectrometer 1T (Laboratoire Léon Brillouin, Saclay), which was used with a pyrolytic graphite (PG) monochromator and a PG analyzer. The final neutron energy was fixed at $E_f = 14.7$ meV. The IN20 spectrometer (Institut Laue-Langevin, Grenoble) was used with the FlatCone multianalyzer in order to record (hkl) -maps with different l values at different temperatures and energy transfers. IN20 has also been used in the polarized mode using polarizing Heusler (111) crystals as a monochromator and an analyzer. For the LPA a set of Helmholtz coils was used to guide and orient the neutron polarization. LPA offers the possibility of distinguishing between nuclear and magnetic scattering and it furthermore allows the separation of the two magnetic components perpendicular to the scattering vector. Generally, nuclear scattering is a non-spin-flip (NSF) process regardless of the initial neutron polarization state. Only magnetic components perpendicular to the scattering vector ($\mathbf{Q} \parallel x$ by definition) are accessible in a neutron experiment. The components perpendicular to the polarization axis (y being in the scattering plane and z being the perpendicular axis of the spectrometer) contribute to the spin-flip (SF) channel, while those parallel to the axis of polarization scatter into the NSF channel.

The PUMA spectrometer (FRM-II, Garching) was used with a PG monochromator and a PG analyzer with a fixed final neutron energy of $E_f = 14.7$ meV. High energy transfers were measured at the time-of flight spectrometer MAPS (Rutherford-Appleton Laboratory, Didcot). The incident beam energies were $E_i = 55$ and 100 meV with k_i parallel to the c axis. The measured intensities were normalized to absolute units by using a vanadium standard (with 30% error).

III. RESULTS AND DISCUSSION

A. Generalized susceptibility of LiFeAs in an absolute scale

In order to express the dynamic susceptibility of LiFeAs in absolute units data taken on the time-of-flight spectrometer MAPS and triple-axis spectrometer data from the 1T instrument were used yielding perfect agreement. The time-of-flight data can be normalized by com-

parison with incoherent scattering from a vanadium sample and with the sample mass. This procedure is well-established at the MAPS instrument and described in large detail in reference.²² In contrast the normalization of triple-axis data is more complex as the resolution function and the beam profile are more structured. Here we follow the most common way to normalize the magnetic scattering by comparison with phonon measurements on the same sample. This method, furthermore, excludes mistakes arising from impurity phases.

The scattering potential of the sample is discussed in terms of the double-differential cross section $\frac{d^2\sigma}{d\Omega dE'}$ with E' the final energy. In any INS experiment this entity is folded with the resolution and transmittance function of the instrument. We use the RESLIB programs²³ to quantitatively analyse the scattering intensities. In our experiment a neutron monitor between the monochromator and the sample is used to scale the detector counts into the entity counts per given monitor (note that this monitor is corrected for higher order contaminations). The calculation splits the instrumental effects in the finite Gaussian resolution and a transmittance term. The intrinsic double differential cross section is first folded with the Gaussian resolution in the four-dimensional space consisting of \mathbf{Q} -space and energy, see Eq. 1. Here $\mathbf{M}(\mathbf{Q}, \omega)$ is the resolution matrix according to the Popovici approximation²⁴ and Δ the four-dimensional difference vector consisting of the \mathbf{Q} -space coordinates and energy, see Eq. 2.

$$\frac{d^2\tilde{\sigma}}{d\Omega dE'}(\mathbf{Q}, \omega) = \int \int \int \int d^3Q' d\omega' \frac{d^2\sigma}{d\Omega dE'}(\mathbf{Q}', \omega') \cdot \exp\left(-\frac{1}{2}[\Delta \cdot \mathbf{M}(\mathbf{Q}, \omega) \cdot \Delta^T]\right) \quad (1)$$

$$\Delta := (Q'_x - Q_x, Q'_y - Q_y, Q'_z - Q_z, \omega' - \omega) \quad (2)$$

In order to calculate the intensity in the detector one has to multiply the folded double cross section with a normalization factor $R_0(\mathbf{Q}, \omega)$ describing amongst others the efficiency of the secondary spectrometer and the resolution function normalization $(2\pi)^{-2} \sqrt{\det \mathbf{M}}$. In contrast to the RESLIB manual we do not include the $\frac{k_f}{k_i}$ factor to R_0 but follow the common practice keeping this factor in the double-differential cross section.^{25,26}

$$I(\mathbf{Q}, \omega) = c \cdot R_0(\mathbf{Q}, \omega) \cdot \frac{d^2\tilde{\sigma}}{d\Omega dE'}(\mathbf{Q}, \omega) = c \cdot \frac{d^2\tilde{\sigma}}{d\Omega dE'}(\mathbf{Q}, \omega) \quad (3)$$

For known resolution and transmission functions the study of a predictable signal allows one to determine the scale factor c describing amongst others the effective sample size. The transformed double-differential cross section $\frac{d^2\tilde{\sigma}}{d\Omega dE'}(\mathbf{Q}, \omega)$ thus contains the intrinsic scattering strength of the system combined with the spectrometer properties.

We use the scattering by an acoustic phonon for normalization. The single-phonon cross section is given by

Eq. 4 (Refs. 25,26) where $n(\omega) + 1$ is the Bose population factor for neutron energy loss. $F_{dyn}(\mathbf{Q})$ denotes the dynamical structure factor of the particular phonon mode at this scattering vector, which can be calculated with the help of a lattice-dynamical model, see Eq. 5. The δ function in Eq. 6 is approximated in the calculation by a Lorentzian profile with finite half width. The symbols in Eqs. 4-6 follow the same convention as in Refs. 25,26.

$$\begin{aligned} \frac{d^2\sigma}{d\Omega dE'}(\mathbf{Q}, \omega) &= N \cdot \frac{k_f}{k_i} \cdot \frac{n(\omega) + 1}{2\omega(q)} \cdot |F_{dyn}(\mathbf{Q})|^2 \cdot \delta(\omega - \omega(q)) \\ &= N \cdot \frac{k_f}{k_i} \cdot \frac{n(\omega) + 1}{2\omega(q)} \cdot |F_{dyn}(\mathbf{Q})|^2 \cdot \hbar \delta(E - E(q)) \end{aligned} \quad (4)$$

$$F_{dyn}(\mathbf{Q}) = \sum_d \frac{b_d}{\sqrt{m_d}} \cdot e^{-i\mathbf{Q} \cdot \mathbf{r}_d} \cdot \mathbf{Q} \cdot \hat{\mathbf{e}}(\mathbf{q}) \cdot e^{-W_d(Q)} \quad (5)$$

For an acoustic phonon close to the Brillouin-zone center one may further simplify the calculation as all atoms in the primitive cell are parallel polarized with components $\frac{\sqrt{m_d}}{\sqrt{M_{tot}}}$ (here m_d and M_{tot} denote the individual and total masses, respectively). The dynamic structure factor then corresponds to that of the nuclear Bragg reflection multiplied by the length of the scattering vector, Q , the inverse square root of the total mass and by the cosine of the angle between scattering vector and phonon polarization, $\cos(\alpha)$. The latter factor is close to one in a reasonably chosen scan.

$$F_{dyn}(\mathbf{Q}) = \frac{Q \cdot \cos(\alpha)}{\sqrt{M_{tot}}} \sum_d b_d \cdot e^{-i[\mathbf{Q} \cdot \mathbf{r}_d + W_d(Q)]} \quad (6)$$

The double differential cross section of the phonon scattering is obtained by subtracting the (refined) background from the raw data and then by dividing by the (refined) scale factor. The phonon dispersion is described by a simple linear relation, $\omega = c \cdot |q|$. Fitting the phonon cross-section with its intensity prefactors to the raw data using the RESLIB code yields a scale factor of 13.1(8) and a constant background of 2 counts per monitor. The raw data can therefore be converted into an absolute scale that still contains the resolution functions of the instrument, see the right axis of ordinate in Fig. 1.

In order to evaluate the magnetic signal we start with the autocorrelation of the spin Fourier coefficients $S_{\mathbf{Q}}^{\alpha}(t)$, here α, β denote the space indices, γ the neutron gyromagnetic factor, e the electron charge, m_e the electron mass, c the speed of light, $f(Q)$ the magnetic form factor at the scattering vector, g the Landé factor and $\delta_{\alpha\beta}$ the Kronecker symbol. Note that the second line of Eq. 7 has the unit of an inverse energy (eV^{-1}).

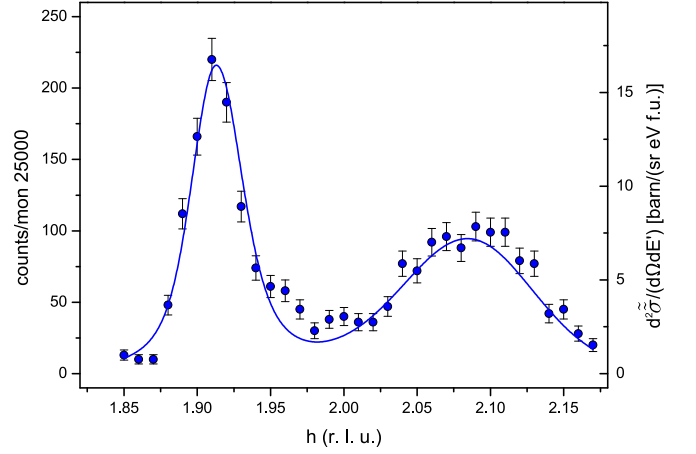


FIG. 1: (Color online) Raw data showing the transversal \mathbf{q} -scan across the (220) phonon at $T = 3.5$ K an energy transfer of 4.5 meV measured at the 1T spectrometer. The scattered intensity is given in counts/(monitor 25000) on the left ordinate and in absolute cross section values on the right ordinate for the folded cross section $\frac{d^2\sigma}{d\Omega dE'}(\mathbf{Q}, \omega)$.

$$\begin{aligned} \frac{d^2\sigma}{d\Omega dE'}(\mathbf{Q}, \omega) &= \left(\frac{\gamma e^2}{m_e c^2} \right)^2 \left(\frac{gf(Q)}{2} \right)^2 \frac{k_f}{k_i} e^{-2W(Q)} \\ &\cdot \sum_{\alpha\beta} (\delta_{\alpha\beta} - \hat{Q}_\alpha \hat{Q}_\beta) \frac{1}{2\pi\hbar} \int_{-\infty}^{\infty} dt \cdot e^{-i\omega t} \langle S_{\mathbf{Q}}^{\alpha}(0), S_{\mathbf{Q}}^{\beta}(t) \rangle \end{aligned} \quad (7)$$

With the fluctuation dissipation theorem one may transform the cross section to the imaginary part of the generalized dynamic susceptibility, which we assume here to be isotropic in spin space.

$$\begin{aligned} \frac{d^2\sigma}{d\Omega dE'}(\mathbf{Q}, \omega) &= \left(\frac{\gamma e^2}{m_e c^2} \right)^2 \left(\frac{gf(Q)}{2} \right)^2 \frac{k_f}{k_i} e^{-2W(Q)} \\ &\cdot \frac{N}{\pi(g\mu_B)^2} [n(\omega) + 1] \cdot 2 \cdot \chi''(\mathbf{Q}, \omega) \end{aligned} \quad (8)$$

A susceptibility can be given in various units creating considerable confusion but here the unit problem drops out due to the term Bohr-magneton, μ_B , squared in the denominator. The natural microscopic unit to discuss the susceptibility is thus μ_B^2/eV per formula unit, which we will use in the following.

Deducing the absolute scale of the cross section of the magnetic fluctuation is now obtained in the same way as in the phonon case by subtracting the background and by dividing by the scale factor obtained from the phonon fit. However, in order to fit the data and deduce the background a model is needed to describe the generalized susceptibility $\chi''(\mathbf{q}, \omega)$. We assume a superposition of single relaxor functions (Eq. 9) in energy with

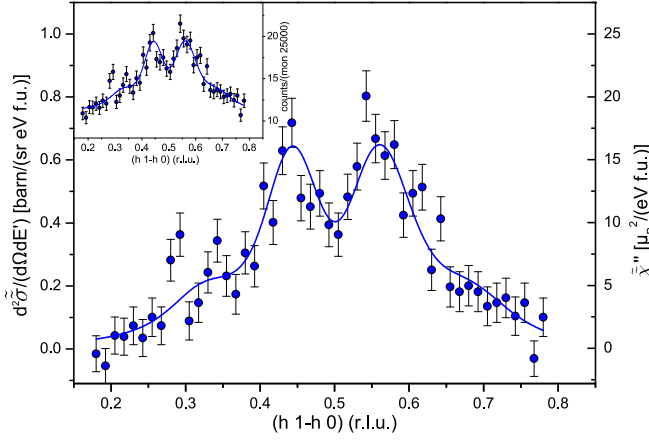


FIG. 2: (Color online) Incommensurate antiferromagnetic fluctuations at $T = 3.5$ K and at an energy transfer of 5 meV measured at the 1T spectrometer. The ordinates are given in absolute units of cross section (left) or of the generalized susceptibility (right). The inset shows the raw magnetic data before subtraction of the background and the division by the scale factor.

a Lorentzian q -dependence centered at the four positions $\mathbf{q}_c = (0.5 \pm \delta_1, 0.5 \mp \delta_1, 0)$ and $(0.5 \pm \delta_2, 0.5 \mp \delta_2, 0)$. We take only the in-plane components of \mathbf{q} into account. δ_1 (δ_2) is the incommensurability of 0.057(3) r.l.u. [0.17(2) r.l.u.] (see Sec. III B for a detailed description of the two signals) and the HWHM was refined to $\xi_1 = 0.042(9)$ r.l.u. [$\xi_2 = 0.07(3)$], which yields the best agreement with the experimental data.

$$\chi''(\mathbf{q}, \omega) = \chi'(\mathbf{q}_c, 0) \cdot \frac{\xi^2}{(\mathbf{q} - \mathbf{q}_c)^2 + \xi^2} \frac{\Gamma \hbar \omega}{(\hbar \omega)^2 + \Gamma^2} \quad (9)$$

In a first step, the constant background (11 counts per monitor 25000 \sim 20 s) was determined and subtracted from the raw data which was then divided by the scale factor deduced from the phonon fit yielding the transformed double-differential cross section $\frac{d^2\tilde{\sigma}}{d\Omega dE'}(\mathbf{Q}, \omega)$. From this one may obtain a susceptibility folded with the instrument resolution and transmission by dividing by all the intensity prefactors in Eq. 8; this result is shown in Fig. 2 on the right coordinate axis. The intrinsic strength and shape of $\chi''(\mathbf{q}, \omega)$, however, can only be obtained by fitting the model, Eq. 9, to the raw data (a value of 10.9 meV has been used for Γ obtained by the single-relaxor fit to the data presented in Sec. III B). Thereby we obtain $\chi'(\mathbf{q}_c, 0) = 7.4(8)$ and $35(1) \mu_B^2/\text{eV}$ at the outer and inner incommensurate positions, respectively, see Fig. 2.

B. Evidence for additional contributions to magnetic scattering

The incommensurate fluctuation has been reinvestigated at the thermal triple-axis spectrometer PUMA

(FRM-II, Garching). Fig. 3 shows transverse q -scans across the $(0.5, 0.5, 0)$ position at different energy transfer clearly documenting a complex Q-shape of the magnetic response. The incommensurate magnetic correlations exhibit at least an asymmetric profile with pronounced shoulders towards larger incommensurability (compared to the $(0.5, 0.5, q_l)$ center). Therefore, the data have been described with two pairs of symmetrical Gaussian functions on a constant background. Note that parts of the data are contaminated by phonon scattering towards lower energy transfer for which these data points are not shown. The resulting fit curves [(red) solid lines] show a very good agreement with the raw data, while the dashed (dash-dotted) curves indicate the contribution of the signal at $Q_{inc,1} \approx (0.43, 0.57, 0)$ [$Q_{inc,2} \approx (0.35, 0.65, 0)$].

Angle resolved photoemission spectroscopy (ARPES) experiments^{2,11} have revealed the Fermi surface to consist of two similarly sized electron-like sheets around the X point and hole-like sheets around the Γ point. In Ref. 21 the authors have identified the INS signal to be connected to scattering between the outer hole pocket and the electron pockets by using a simple tight-binding fit to the ARPES data, while involvement of the inner hole pocket was concluded in Ref. 20. Deeper understanding of the nesting signal requires the analysis of the orbital character of the various Fermi surface sheets which essentially arise from the t_{2g} d_{xz} , d_{yz} and d_{xy} orbitals.^{27,28} There seems to be agreement that the outer hole pocket can be identified with d_{xy} orbital character which also contributes to the electron pockets. The d_{xy} states should result in two-dimensional bands, but d_{xz} and d_{yz} contributions yield considerable dispersion along the perpendicular directions and strong q_z modulation of the Fermi surfaces.^{27,28} If one associates the nesting magnetic correlations exclusively with d_{xy} orbitals it appears difficult to understand a split signal but an asymmetry or a shoulder can arise from a peculiar detail of the Fermi surface shape that is not sufficiently well understood so far. Sr_2RuO_4 is a well studied example with incommensurate magnetic correlations arising from Fermi-surface nesting,²⁹ and this material also exhibits an asymmetric magnetic response with a shoulder. Quite recently four theoretical papers aimed to quantitatively model the variation of the superconducting gap on the Fermi surface sheets arriving at contradictory results.^{30–33} The quantitative description of magnetic excitations by analyzing transitions between states with the same or different orbital character will help to arrive at a better understanding of the electronic structure of LiFeAs .

The peak intensities of $Q_{inc,1}$ and $Q_{inc,2}$ have been followed as a function of energy above and below T_C . As it can be seen in Fig. 4 the main signal $Q_{inc,1}$ shows the same dependence as already reported in Ref. 19 with a crossover between the scattered intensity below and above T_C at 4.5 meV and an increase of intensity above 7-8 meV. On the other hand the intensity at $Q_{inc,2}$ suggests a different behaviour in dependence on the energy transfer. The scattered intensity at 20 K stays above the

one at 5 K up to an energy transfer of roughly 7 meV, above which the value $I(T < T_C)$ becomes stronger than $I(T > T_C)$. The different energy dependences of the signals at $Q_{inc,1}$ and $Q_{inc,2}$ strengthen the assumption of their independent origin and can be explained due to different gap values on different parts of the Fermi surface.

The derived amplitude of the excitation at $Q_{inc,1}$ has been corrected for the monitor and the Bose factor yielding the imaginary part of the generalized susceptibility which is shown in Fig. 5. The data have been fitted with single-relaxor functions. The data does not allow to state a clear tendency of the critical energy, however, a clear reduction of $\chi''(Q_{inc}, E)$ towards higher temperatures is observable. In addition the incommensurate magnetic correlations become strongly broadened at the temperature of only 100 K where the two peak structure has already changed into a broad plateau.

By using the triple-axis spectrometer IN20 in combination with the Flatcone multianalyzer, planar sections of the reciprocal space can be recorded by simple 2θ scans which are afterwards converted into \mathbf{Q} -space. As theory predicts that a ferromagnetic instability may dominate at higher temperatures and/or higher energies,¹⁵ maps of the reciprocal space have been recorded up to 150 K and an energy transfer of 40 meV focusing on the (100) and (110) positions. However, our obtained data does not give any hint for ferromagnetic fluctuations in LiFeAs.

C. Spin space anisotropy of magnetic correlations

The IN20 spectrometer has then been used with polarized neutrons whose polarization axis after the scattering process has been analyzed. The observation of the incommensurate signal in the SF channels proves its magnetic origin (Note that the SF background has been subtracted according to the description in Ref. 34). The peak intensity at the point $\mathbf{Q}=(0.43\ 0.57\ 0)$ has been measured as a function of the energy transfer for the SF_y and SF_z channels (Fig. 6). Although only the SF_y channel has been measured with high statistics a slight spin-space anisotropy of the magnetic fluctuation is visible between 6 and 12 meV, where the out-of-plane fluctuation lies above the in-plane fluctuation similar to observations in electron doped BaFe_2As_2 ^{35–37}. However, the spin-space anisotropy in LiFeAs needs further experimental corroboration by measuring the other channels with better statistics.

In order to reveal eventual weak ferromagnetic fluctuations a \mathbf{q} -scan across $\mathbf{Q}=(110)$ at $T = 150$ K and $E = 12$ meV has been carried out. All three SF channels revealed neutron counts similar to the SF background meaning that no significant magnetic scattering is present.

D. High-energy magnetic response

Due to the limitation of triple-axis spectrometers concerning the incident energy, high energy transfers have to be measured using a time-of-flight spectrometer. However, higher incident energies are at the cost of a loss in resolution. With the c axis of the sample aligned along the incident beam one obtains a projection of $S(\mathbf{Q}, \omega)$ along this axis after the measurement of a curved 3-dimensional hypersurface in the 4-dimensional manifold of reciprocal space. In the projection the l component is an implicit variable which changes with energy transfer, nevertheless being calculable, i.e. the obtained data is three-dimensional in (h, k, E) -space. In order to visualize the data the program MSLICE has been used which offers the possibility of averaging the data along a chosen axis to produce a slice or integrating along two axes to produce a cut. By measuring a standard vanadium sample with known mass the intensity can be normalized to an absolute scale in mb/(sr meV f.u.) by using the sample mass and molar mass. Fig. 7(a) shows a slice of the $(hk0)$ plane which has been integrated between 10 meV and 30 meV for an incident beam energy of 55 meV. Two peaks can be observed around the $(0.5\ 0.5\ 0)$ position. By integrating the data perpendicular to the scan path indicated by the dashed line, one obtains the curve shown in Fig. 7(b) clearly revealing the incommensurability of the antiferromagnetic fluctuations. However, also the time-of-flight data indicates an asymmetric shape or an additional signal at larger incommensurability. Two pairs of symmetrical Gaussian functions on a constant background have been fitted to the data, from which the incommensurabilities $\delta_1 = 0.061(3)$ and $\delta_2 = 0.17(1)$ could be extracted. The value of δ_1 is in good agreement with our previous results.¹⁹ Note that the absolute intensity scale obtained by the renormalization to a vanadium standard (between 10 and 30 meV) is in very good agreement with our results shown in Sec. III A (Fig. 2, 5 meV) and also with a report on polycrystalline samples.³⁸ In order to investigate the magnetic signal at higher energy transfers an incident neutron energy of 100 meV has been used. Fig. 8 shows $(hk0)$ slices of 10 meV thickness each. The magnetic fluctuation can be observed around the $(0.5\ 0.5\ 0)$ point, but the loss in resolution becomes evident. However, there is a significant signal which can be separated from the background up to an energy transfer of 60 meV. For the slice in Fig. 8(f) the signal is reduced to the background. Due to the limited \mathbf{Q} -resolution in comparison to $E_i=55$ meV the incommensurability could not be investigated at higher energy transfers.

IV. CONCLUSION

In summary we have extended our previous work concerning the characterization of the incommensurate antiferromagnetic fluctuations in LiFeAs. Time-of-flight experiments show that the magnetic signal is observable up

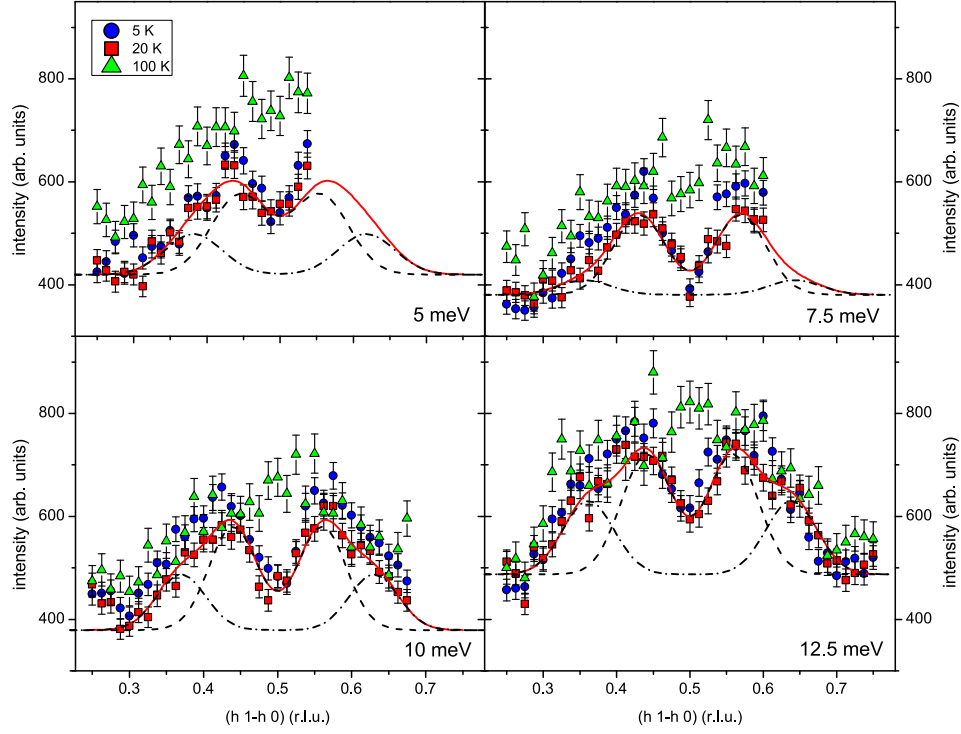


FIG. 3: (Color online) Transverse q-scans across $(0.5\ 0.5\ 0)$ at different energy transfers measured at the PUMA spectrometer. The data have been fitted by two pairs of symmetrical Gaussians on a constant background. A phonon contamination is visible towards smaller energy transfer, for which those data points have been omitted. Especially at higher energy transfers the data indicate an additional signal at larger incommensurability (dash-dotted line) besides the signal at $(0.43\ 0.57\ 0)$ (dashed line).

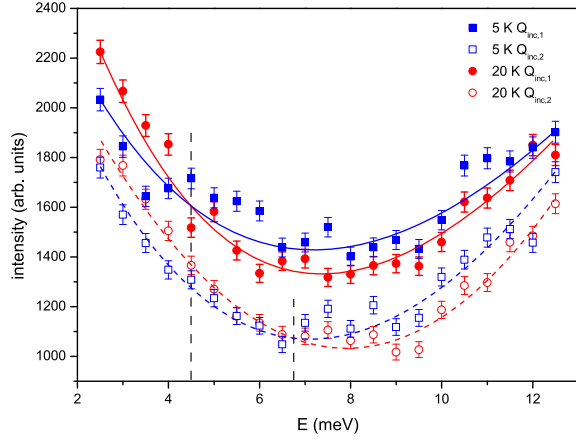


FIG. 4: (Color online) Energy dependence of the INS scattering at $Q_{inc,1}=(0.425\ 0.575\ 0)$ and $Q_{inc,2}=(0.35\ 0.65\ 0)$ measured at the PUMA spectrometer. The dashed lines indicate where the scattered intensities of the normal [(red) circles] and superconducting state [(blue) squares] cross.

to energy transfers of 60 meV, while the incommensurability remains unchanged up to 30 meV (measurements of higher energy transfers were at the cost of resolution prohibiting a quantitative analysis of the incommensurability). Longitudinal polarization analysis proved the magnetic origin of the observed signal and an eventual

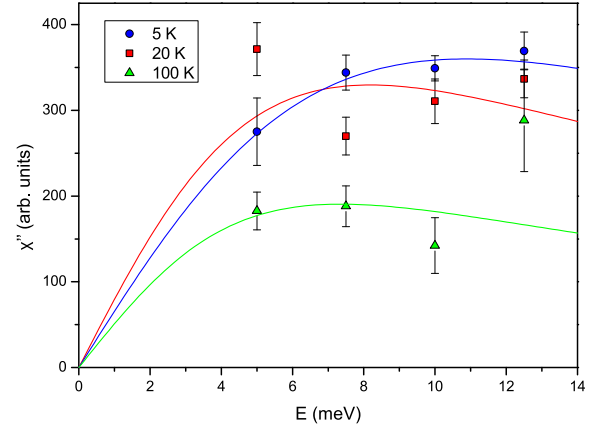


FIG. 5: (Color online) Imaginary part of the generalized susceptibility at 5 K, 20 K and 100 K as obtained by the amplitude from the fits to the data shown in Fig. 3 and correction for the monitor and the Bose factor. The solid lines represent fits by a single relaxor functions $\chi''(Q_{inc,1}, E) = \chi'(Q_{inc,1}, 0) \frac{\Gamma E}{\Gamma^2 + E^2}$

spin-space anisotropy between 8 and 10 meV could be deduced that resembles observation in other FeAs-based superconductors.

The asymmetric shape of the incommensurate peak suggests the presence of two different signals which may

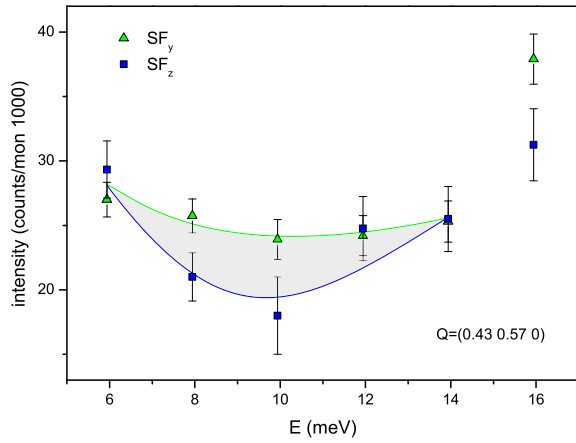


FIG. 6: (Color online) Energy scan of the SF_y and SF_z intensities at $Q=(0.43\ 0.57\ 0)$ measured at the IN20 spectrometer showing a local anisotropy of the magnetic fluctuation between 6 and 12 meV.

correspond to scattering between the outer hole pocket and the inner electron pocket as well as between the outer hole pocket and the outer electron pocket. The different energy dependences of the peak intensities of $Q_{inc,1}$ and $Q_{inc,2}$ support the picture of two independent signals. Furthermore, we have converted the intensity of the scattered neutrons into an absolute scale making it possible to compare the strength of the magnetic

fluctuations in LiFeAs with those of related compounds. Nearly optimally Co-doped $BaFe_2As_2$ yields a maximum value of roughly 7.5 mb/(sr meV Fe) at the resonance feature (Ref. 39). By averaging the peak values of the triple-axis (Fig. 2) and time-of-flight data (Fig. 7) we obtain 0.95 mb/(sr meV Fe) rendering the low-temperature fluctuations in LiFeAs by a factor 8 weaker than the magnetic resonance in Co-doped $BaFe_2As_2$. This perfectly agrees with our earlier work,¹⁹ where we estimated the same ratio between the incommensurate fluctuations in LiFeAs and the commensurate resonance in $Ba(Fe_{0.92}Co_{0.08})_2As_2$ by normalizing the magnetic signal to the respective phonon signal. Due to the incommensurability a factor of two is recovered for which the magnetic scattering per Fe ion in LiFeAs is by roughly a factor four weaker than the respective scattering in nearly optimally Co-doped $BaFe_2As_2$ which must be reconciled with the fact that the superconducting transition temperature is only little reduced in LiFeAs.

Acknowledgments

This work was supported by the Deutsche Forschungsgemeinschaft (DFG) through the Priority Programme SPP1458 (Grants No. BE1749/13, BU887/15-1 and BR2211/1-1). S.W. thanks the DFG for funding in the Emmy Noether Programme (project 595/3-1).

- * Corresponding author. Electronic address: qureshi@ph2.uni-koeln.de
- † Electronic address: braden@ph2.uni-koeln.de
- ¹ Y. Kamihara, T. Watanabe, M. Hirano, and H. Hosono, *J. Am. Chem. Soc.* **130**, 3296 (2008).
 - ² A. A. Kordyuk, V. B. Zabolotnyy, D. V. Evtushinsky, T. K. Kim, I. V. Morozov, M. L. Kubic, R. Follath, G. Behr, B. Büchner, and S. V. Borisenko, *Phys. Rev. B* **83**, 134513 (2011).
 - ³ J. W. Lynn, and P. C. Dai, *Physica (Amsterdam)* **469C**, 469 (2009).
 - ⁴ M. Rotter, M. Tegel, and D. Johrendt, *Phys. Rev. Lett.* **101**, 107006 (2008).
 - ⁵ A. S. Sefat, R. Jin, M. A. McGuire, B. C. Sales, D. J. Singh, and D. Mandrus, *Phys. Rev. Lett.* **101**, 117004 (2008).
 - ⁶ P. Alireza, Y. T. C. Ko, C. M. P. J. Gillett, J. M. Cole, G. G. Lonzarich, and S. E. Sebastian, *J. Phys.: Condens. Matter* **21**, 012208 (2009).
 - ⁷ J. H. Tapp, Z. Tang, B. Lv, K. Sasmal, B. Lorenz, P. C. W. Chu, and A. M. Guloy, *Phys. Rev. B* **78**, 060505(R) (2008).
 - ⁸ X. C. Wang, Q. Q. Liu, Y. Lv, W. B. Gao, L. Yang, R. C. Yu, F. Y. Li, and C. Q. Jin, *Solid State Commun.* **148**, 538 (2008).
 - ⁹ M. J. Pitcher, D. R. Parker, P. Adamson, S. J. C. Herkelrath, A. T. Boothroyd, R. M. Ibberson, M. Brunelli, and S. J. Clarke, *Chem. Commun.* p. 5918 (2008).
 - ¹⁰ P. M. R. Brydon, M. Daghofer, C. Timm, and J. van den Brink, *Phys. Rev. B* **83**, 060501(R) (2011).

- ¹¹ S. V. Borisenko, V. B. Zabolotnyy, D. V. Evtushinsky, T. K. Kim, I. V. Morozov, A. N. Yaresko, A. A. Kordyuk, G. Behr, A. Vasiliev, R. Follath, et al., *Phys. Rev. Lett.* **105**, 067002 (2010).
- ¹² T. Hajiri, T. Ito, R. Niwa, M. Matsunami, B. H. Min, Y. S. Kwon, and S. Kimura, *Phys. Rev. B* **85**, 094509 (2012).
- ¹³ M. P. Allan, A. W. Rost, A. P. Mackenzie, Y. Xie, J. C. Davis, K. K. C. H. Lee, A. Iyo, H. Eisaki, and T.-M. Chuang, *Science* **336**, 563 (2012).
- ¹⁴ D.-J. Jang, J. B. Hong, Y. S. Kwon, T. Park, K. Gofryk, F. Ronning, J. D. Thompson, and Y. Bang, *Phys. Rev. B* **85**, 180505(R) (2012).
- ¹⁵ C. Platt, R. Thomale, and W. Hanke, *Phys. Rev. B* **84**, 235121 (2011).
- ¹⁶ T. Hänke, S. Sykora, R. Schlegel, D. Baumann, L. Harnagea, S. Wurmehl, M. Daghofer, B. Büchner, J. van den Brink, and C. Hess, *Phys. Rev. Lett.* **108**, 127001 (2012).
- ¹⁷ S. H. Baek, H. J. Grafe, F. Hammerath, M. Fuchs, C. Rudisch, L. Harnagea, S. Aswartham, S. Wurmehl, J. van den Brink, and B. Büchner, *Eur. Phys. J. B* **85**, 159 (2012).
- ¹⁸ S. H. Baek, L. Harnagea, S. Wurmehl, B. Büchner, and H. J. Grafe, *J. Phys.: Condens. Matter* **25**, 162204 (2013).
- ¹⁹ N. Qureshi, P. Steffens, Y. Drees, A. C. Komarek, D. Lamago, Y. Sidis, L. Harnagea, H.-J. Grafe, S. Wurmehl, B. Büchner, et al., *Phys. Rev. Lett.* **108**, 117001 (2012).
- ²⁰ M. Wang, M. Wang, H. Miao, S. Carr, D. L. Abernathy, M. B. Stone, X. C. Wang, L. Xing, C. Q. Jin, X. Zhang, et al., *Phys. Rev. B* **86**, 144511 (2012).

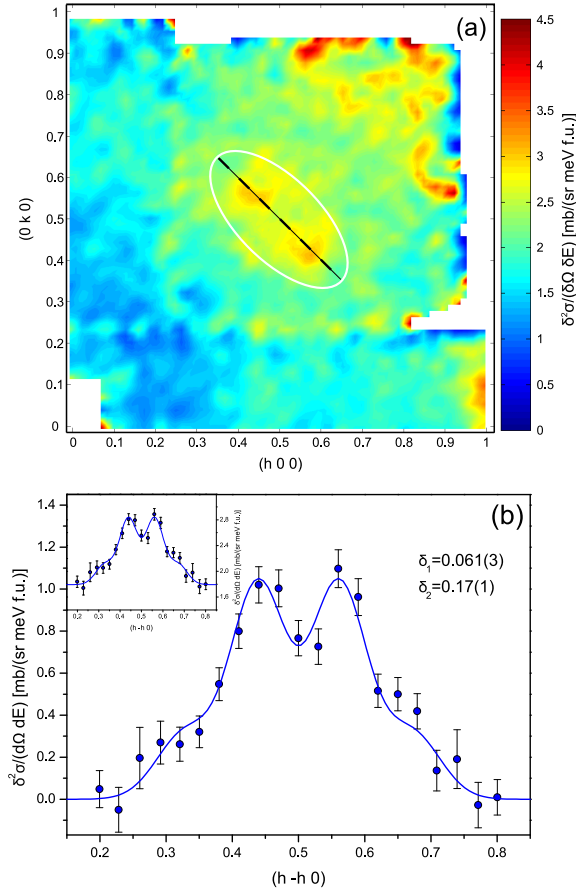


FIG. 7: (Color online) (a) Time-of-flight data showing $S(\mathbf{Q}, \omega)$ in the $(hk0)$ plane integrated between 10 meV and 30 meV ($E_i=55$ meV, $T=10$ K). The incommensurate peaks are marked by a white ellipse. The black dashed indicates the cut along the $[h -h 0]$ direction shown in (b). The fit of two pairs of symmetrical Gaussian functions after the subtraction of a constant background (determined from the fit in the inset) yields the incommensurabilities $\delta_1 = 0.061(3)$ and $\delta_2 = 0.17(1)$.

²¹ J. Knolle, V. B. Zabolotnyy, I. Eremin, S. V. Borisenko,

- N. Qureshi, M. Braden, D. V. Evtushinsky, T. K. Kim, A. A. Kordyuk, S. Sykora, et al., Phys. Rev. B **86**, 174519 (2012).
- ²² G. Xu, Z. Xu, and J. M. Tranquada, Rev. Sci. Instrum. **84**, 083906 (2013).
- ²³ A. Zheludev, RESLIB 3.4c (Oak Ridge National Laboratory, Oak Ridge, TN) (2006).
- ²⁴ M. Popovici, Acta Crystallogr., Sect. A: Found. Crystallogr. **31**, 507 (1975).
- ²⁵ W. Marshall and S. Lovesey, *Theory of thermal Neutron Scattering* (Oxford University Press, 1971).
- ²⁶ G. L. Squires, *Introduction to the theory of thermal neutron scattering* (Dover Publications Inc., 1997).
- ²⁷ Z. P. Yin, K. Haule, and G. Kotliar, Nat. Mater. **10**, 932 (2011).
- ²⁸ J. Ferber, K. Foyevtsova, R. Valentí, and H. O. Jeschke, Phys. Rev. B **85**, 094505 (2012).
- ²⁹ M. Braden, Y. Sidis, P. Bourges, P. Pfeuty, J. Kulda, Z. Mao, and Y. Maeno, Phys. Rev. B **66**, 064522 (2002).
- ³⁰ Y. Wang, A. Kreisel, V. B. Zabolotnyy, S. V. Borisenko, B. Büchner, T. A. Maier, P. J. Hirschfeld, and D. J. Scalapino, Phys. Rev. B **88**, 174516 (2013).
- ³¹ Z. P. Yin, K. Haule, and G. Kotliar, arXiv:1311.1188.
- ³² F. Ahn, I. Eremin, J. Knolle, V. B. Zabolotnyy, S. V. Borisenko, B. Büchner, and A. V. Chubukov, arXiv:1402.2112.
- ³³ T. Saito, S. Onari, Y. Yamakawa, H. Kontani, S. V. Borisenko, and V. B. Zabolotnyy, arXiv:1402.2398.
- ³⁴ N. Qureshi, P. Steffens, S. Wurmehl, S. Aswartham, B. Büchner, and M. Braden, Phys. Rev. B **86**, 060410(R) (2012).
- ³⁵ P. Steffens, C. H. Lee, N. Qureshi, K. Kihou, A. Iyo, H. Eisaki, and M. Braden, Phys. Rev. Lett. **110**, 137001 (2013).
- ³⁶ M. Liu, C. Lester, J. Kulda, X. Lu, H. Luo, M. Wang, S. M. Hayden, and P. Dai, Phys. Rev. B **85**, 214516 (2012).
- ³⁷ H. Luo, M. Wang, C. Zhang, X. Lu, L.-P. Regnault, R. Zhang, S. Li, J. Hu, and P. Dai, Phys. Rev. Lett. **111**, 107006 (2013).
- ³⁸ A. E. Taylor, M. J. Pitcher, R. A. Ewings, T. G. Perring, S. J. Clarke, and A. T. Boothroyd, Phys. Rev. B **83**, 220514(R) (2011).
- ³⁹ C. Lester, J.-H. Chu, J. G. Analytis, T. G. Perring, I. R. Fisher, and S. M. Hayden, Phys. Rev. B **81**, 064505 (2010).

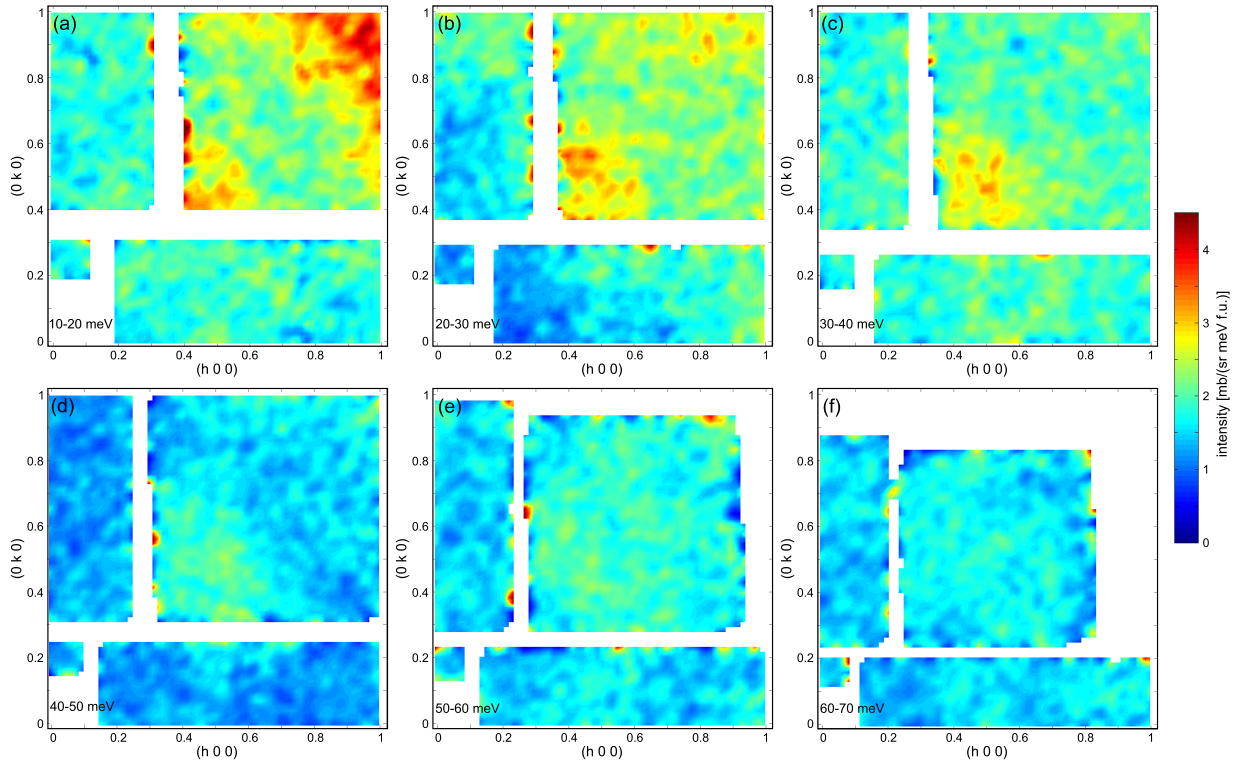


FIG. 8: (Color online) (a)-(f) $S(\mathbf{Q}, \omega)$ in different energy slices from 10-20 meV up to 60-70 meV ($E_i=100$ meV, $T=10$ K). The magnetic signal is observable up to 50-60 meV before it is reduced to the background at higher energies.